



Multidisciplinary Design Optimization of Blended Wing-Body Aircraft with Lateral-Directional Stability Constraints

Cindy Chen*

Institute for Aerospace Studies, University of Toronto, 4925 Dufferin St, Toronto, ON M3H 5T6

Aiden L. Gray†

Université de Moncton, 18 Antonine-Maillet Ave, Moncton, New Brunswick, E1A 3E9, Canada

David W. Zingg‡

Institute for Aerospace Studies, University of Toronto, 4925 Dufferin St, Toronto, ON M3H 5T6

A persistent challenge in the design and adoption of blended-wing-body (BWB) aircraft is maintaining adequate handling qualities across the flight envelope without relying on stability augmentation. To date, many multidisciplinary design optimization (MDO) studies of the BWB have focused on longitudinal stability and control characteristics, assuming that postponing vertical surface design negligibly affects the fuel efficiency and key design features. Moreover, several measures of handling qualities depend on dynamic stability derivatives, which are difficult and expensive to compute in high-fidelity optimization studies. In this work, a handling qualities analysis on a regional-class BWB optimized without consideration of lateral-directional stability reveals an unstable Dutch roll mode. To address this deficiency, constraints are imposed on the yaw stiffness and dihedral effect derivatives in a mixed-fidelity MDO problem based on the solution of the Reynolds-averaged Navier-Stokes equations. The objectives are to determine their effects on block fuel burn and the optimal design, and to evaluate their viability as proxy constraints on Dutch roll behaviour. Imposing a minimum yaw stiffness derivative with a reduced dihedral effect derivative produces an aircraft with Level 2 Dutch roll damping, albeit with a 4.1% block fuel burn penalty. Enforcing a minimum yaw stiffness derivative alone brings the Dutch roll damping ratio to Level 3 at a 1.2% cost to block fuel burn.

I. Nomenclature

$C_{n\beta}, N_v$	yaw moment derivative with respect to sideslip angle or side velocity (yaw stiffness)
$C_{l\beta}, L_v$	roll moment derivative with respect to sideslip angle or side velocity (dihedral effect)
$C_{Y\beta}, Y_v$	side force derivative with respect to sideslip angle or side velocity
C_{nr}, N_r	yaw moment derivative with respect to yaw rate (yaw damping)
C_{lr}, L_r	roll moment derivative with respect to yaw rate
C_{Yr}, Y_r	side force derivative with respect to yaw rate
C_{np}, N_p	yaw moment derivative with respect to roll rate
C_{lp}, L_p	roll moment derivative with respect to roll rate (roll damping)
C_{Yp}, Y_p	side force derivative with respect to roll rate
t/c	thickness-to-chord ratio
L/D	lift-to-drag ratio
α	angle of attack
β	sideslip angle
I_{xx}, I_{zz}	mass moment of inertia about the x and z -axis, respectively
I_{xz}	mass product of inertia about the x and z -axes

*PhD Candidate, University of Toronto Institute for Aerospace Studies, cindyq.chen@mail.utoronto.ca

†Assistant Professor, Université de Moncton, aiden.gray@umoncton.ca

‡Distinguished Professor of Computational Aerodynamics and Sustainable Aviation, University of Toronto Institute for Aerospace Studies, AIAA Associate Fellow, david.zingg@utoronto.ca

II. Introduction

COMMERCIAL aviation faces the dual challenge of achieving net zero CO₂ emissions by 2050 while supporting continued growth in passenger transport [1]. As a result, the industry is actively investing in the research and development of novel configurations in pursuit of a step change in fuel efficiency. One candidate is the blended wing-body (BWB), a tailless configuration with a gradual transition from the centerbody to the wings. Together, these features reduce interference and viscous drag. Moreover, the generation of lift by the centerbody and the alignment of lift and weight alleviate the root bending moment, allowing for an increase in span without the typical weight penalty and consequently reducing induced drag [2]. The absence of the conventional empennage further reduces weight and drag.

However, attaining adequate longitudinal handling qualities is challenging due to the absence of the horizontal tail, the primary pitch stability and control (S&C) mechanism. Lateral-directional handling qualities can also be compromised due to the reduced lever arm between the center of gravity (CG) and vertical surfaces [3]. While stability augmentation can compensate for the instabilities, the system must be sufficiently reliable to meet certification requirements by demonstrating that the likelihood of failure is below a certain threshold [4]. Beyond its inherent S&C disadvantages, the BWB is a tightly integrated configuration with strong interdisciplinary design dependencies because the centerbody, wings, and winglets must fulfill the S&C roles normally assigned to the empennage on conventional aircraft. Consequently, physics-based multidisciplinary design optimization (MDO) with high-fidelity aerodynamics modelling and substantial design freedom is particularly useful for operating within the unfamiliar design space. Such an approach is critical to realizing the potential of the configuration, as it enables punitive S&C and other design requirements to be addressed efficiently, performance to be credibly estimated, and key design drivers to be identified.

For much of the BWB's history, handling qualities analysis has been independent of aerodynamic design. In a conceptual MDO study of long-range BWBs, Boeing produced an 800-passenger aircraft that met the mission requirements but was statically unstable and required stability augmentation. They also designed a 450-passenger variant that burned 32% less fuel per seat than the Airbus A380-700 while achieving a static margin of 5% mean aerodynamic chord (MAC) in some flight conditions by changing the spanwise lift distribution with wing washout [2]. Later, in the X-48 program, the scaled X-48B demonstrator was similarly dependent on a fly-by-wire S&C augmentation system [5]. Low-speed directional control proved difficult even with winglet-mounted rudders and outboard split elevons [6].

The advent of high-performance computing prompted a shift towards aerodynamic shape optimization based on the numerical solution of the Reynolds-averaged Navier-Stokes (RANS) equations. With the ability to add S&C constraints to optimization problems, researchers could design the overall aircraft shape to fulfill requirements related to handling qualities. Lyu and Martins [7] performed a single-point twist and section-shape optimization on Boeing's 450-passenger BWB, subject to constraints on trim, CG location, and cruise static margin. Focusing on regional-class BWBs, Reist *et al.* introduced analysis points on the ground at which control is critical, namely directional trim with one engine inoperative (OEI) and takeoff rotation modelled as a minimum pitch acceleration of 3 deg/s² [8]. In addition, they compared the effectiveness of fins and rudders and the performance attained with a narrow centerbody versus the wider classical configuration. Building on this foundation, Gray and Zingg [9] increased the geometric freedom, optimized the cabin positioning within the centerbody, accounted for the pivot-piston landing gear developed by JetZero to facilitate takeoff rotation [10] [11], and imposed a static margin constraint at low speed, which is typically more critical than cruise. In addition, they imposed constraints on takeoff field length and initial climb to help size the planform and engines, thus studying the impact of many critical design requirements on regional-class BWB performance and design. The substantial aerodynamic design freedom enabled the optimized benchmark aircraft to attain a cruise lift-to-drag ratio of 21.7. Recent work investigating cruise altitudes near 44,500 ft showed lift-to-drag ratios of over 23.7 [12]. Trim requirements at near-stall conditions were also considered, as they are potentially critical for pitch control surface sizing.

A barrier to incorporating handling qualities in high-fidelity MDO is that they are functions of dynamic stability derivatives, whose computation is more costly and memory-intensive than that of their static counterparts [13]. Chang [14] concluded that one optimized BWB from Ref. [15] exhibited inadequate low-speed handling qualities. A Simulink model of the aircraft for real-time flight simulation was built using static aerodynamic data from a RANS flow solver and dynamic stability derivatives from a vortex-lattice solver. The salient findings were that the aircraft studied could not meet Level 1 or 2 requirements from the military standard MIL-STD-1797A [16] without stability augmentation, larger winglets, and spoilers; the critical modes were short-period and Dutch roll, and landing in a 20-knot crosswind was perceived to be more difficult than OEI directional trim at the on-ground minimum control speed.

In a low-to-medium-fidelity MDO study by Gauvrit-Ledogar *et al.* [17], longitudinal criteria from the regulations were evaluated at the CG extremes using stability derivatives from a vortex-lattice solver. Within a high-fidelity optimization framework, Mader and Martins [18] constrained the control anticipation parameter (CAP), a metric for short-period behaviour derived from dynamic stability derivatives calculated using the time-spectral adjoint method,

which assumes a periodic unsteady flow. Also focusing on the CAP, Cosenza and Vos [19] proposed an inverse design procedure based on the modified Routh-Hurwitz stability criterion to limit the design space to regions with the desired range of short-period eigenvalues. Joosten *et al.* [20] set bounds on the roll, yaw, and sideslip angles achieved by the Flying-V based on European regulations for large aircraft [21]. Lateral-directional maneuvers were simulated at the required airspeeds to ensure the aircraft could be controlled to remain within the bounds. Alternatively, several authors have attempted to address the problem from a control standpoint. Applying modern control theory, Cai *et al.* [22] applied a modified Popov-Belevitch-Hautus test to examine the controllability and stabilizability of the aircraft based on its state matrices. Garmendia *et al.* estimated the actuation power requirements with different static margins given the size and deflection rates of the control surfaces [23]. In a paper that examines the tradeoffs between drag, control authority, actuator weight, and actuation power requirements as a function of elevon layout, the same authors reported that the fuel burn benefit was maximized by placing three elevons of unequal span fractions on each wing [24]. Denieul *et al.* [25] optimized the control law gains along all three flight axes while minimizing control surface area, thereby minimizing actuator weight and power consumption.

This paper proposes and evaluates static proxies for dynamic lateral-directional handling qualities, with an emphasis on Dutch roll. Constraints on the yaw stiffness and dihedral effect derivatives are added to mixed-fidelity MDO problems on a regional-class BWB to fulfill two objectives. The first is to determine their individual and combined effects on the optimal design and its fuel efficiency, and the second is to evaluate their applicability as proxies for predicting Dutch roll behaviour. The baseline problem formulation and methodology are adopted from [9]. Except for the pivot-piston nose landing gear, current technology is assumed to minimize the uncertainty in the problem formulation. Post-optimization low-speed dynamic stability analyses are performed using a vortex-lattice solver to correlate these constraints with the Dutch roll damping ratio and natural frequency. Ultimately, this work seeks to help mitigate the risks associated with the market adoption of BWBs by contributing design knowledge pertinent to their optimal performance and safety.

III. Methodology

A. Overview of Computational Framework

This section covers the major components of Jetstream [26], the physics-based MDO framework used in this work. Jetstream has been extensively applied to study BWBs and other unconventional aircraft configurations by automating the exploration of the design space. Prior to using Jetstream, an initial geometry is generated using an in-house component-based parametric design toolbox [27], and a structured multiblock grid is created in ANSYS ICEM CFD. Two grids are used in each optimization: a 256-block O-grid for operating points in free air and a variation with 288 blocks that includes a ground plane at which flow tangency is enforced at the freestream velocity. The latter is used only at analysis points where ground effect is considered. Both grids contain approximately 2.1 million nodes, leading to an approximately design-independent drag error of 22% at the optimum that is accounted for in fuel burn calculations.

1. Integrated Geometry Parameterization and Grid Deformation

The integrated geometry parameterization and grid deformation scheme of Hicken and Zingg [28] has been adopted in Jetstream to accommodate large shape changes with low computational cost. The geometry and grid are parameterized by B-spline surfaces and volumes to form a fitting grid 10-100 times coarser than the computational grid. This maps each block of the computational grid to a B-spline volume. As in the computational grid, control points are placed so that regions with significant geometric curvature or detailed flow features have a higher control point density. Based on changes to the surface control points, geometry updates are propagated across the B-spline volumes via a grid deformation scheme based on the linear elasticity equations, and the computational grid is reconstructed based on the parametric location of each grid point within the B-spline volumes. Spatially-varying formulations are used for the Poisson ratio and Young's modulus to preserve the overall grid quality [29].

2. Geometry Control

Jetstream incorporates a free-form and axial deformation scheme for geometry control that enables substantial geometric freedom [30]. The B-spline control points parameterizing the surface are embedded in free-form deformation (FFD) volumes with streamwise-oriented control point stations attached to fixed parametric span locations along a leading-edge-attached B-spline curve known as an axial curve. Moving the axial control points changes global shape variables, namely sweep, span, and dihedral, whereas local shape variables, namely chord, twist, and section shape, are

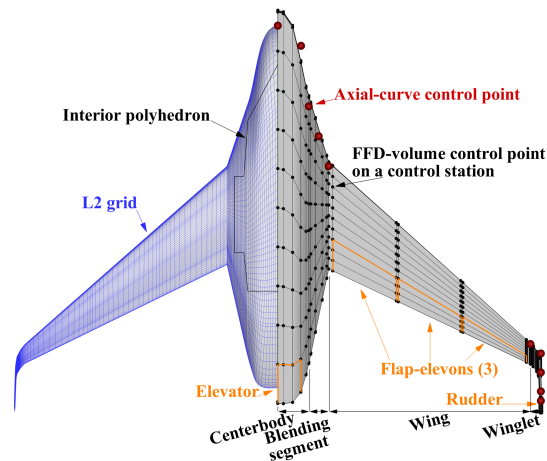


Fig. 1 Geometry control system, with FFD control points in black and axial curve control points in red [9].

controlled by manipulating the FFD control stations. Trailing-edge control surfaces are deflected by rotating the FFD points aft of a specified hinge line across several adjacent stations. In this work, the elevator extends up to 10%-chord from the trailing edge and the flap-elevons and rudder up to 30%-chord. The rudder spans 80% of the winglet height. While the continuity of the outer mold line (OML) is maintained, unlike how control surface deflections on real aircraft create gaps, Reist *et al.* [8] validated this simplified model on an extruded 2D airfoil section [31] and found adequate agreement. Figure 1 shows the planform with the grid overlay, geometry control system, control surface layout, and interior-space polyhedron containing the flight deck, cabin, and cargo holds.

3. Flow Solver

A high-fidelity flow solver is essential for a credible performance assessment of an aircraft flying at transonic speed, as it can model complex flow phenomena such as separation and shock formation as well as every component of drag. A parallel implicit algorithm is used to solve the steady RANS equations closed with the negative variant of the Spalart-Allmaras turbulence model with a quadratic constitutive relation [32, 33]. Spatial discretization is achieved with second-order summation-by-parts operators, and boundary and block-interface conditions are implemented using simultaneous approximation terms. The discretized governing equations are solved using a Newton-Krylov method, where the linear system is preconditioned with the Schur complement.

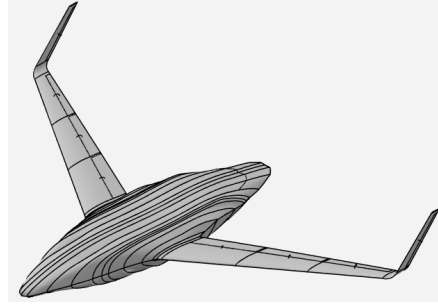
4. Mixed-Fidelity Models for Non-Aerodynamics Disciplines

Significant computational savings can be achieved by modelling non-aerodynamics disciplines at lower fidelity, provided that this level of fidelity is adequate for their specific purpose. Following the approach of Gray and Zingg [9], low-fidelity models are used for propulsion, weight, and drag augmentation, while mass properties and flight mechanics are modelled at medium fidelity. Using a rubber engine model, the engines are sized based on whichever of the three scenarios requires the largest engine: 1) maintaining a 300 ft/min climb at cruise, 2) achieving a 2.4% climb gradient after liftoff, or 3) satisfying a takeoff field length (TOFL) constraint under sea-level conditions. The two engines, which do not ingest the boundary layer, are treated as point masses fixed at one-half nacelle diameter above the nose and one nacelle diameter laterally from the centerline. The wing weight model is that of Torenbeek [34], in which the blending segment and wing are combined into an equivalent trapezoidal wing. The wing weight is then correlated with the span, area, root thickness, and sweep of the equivalent wing, as well as the maximum zero-fuel weight. The winglet weight is estimated based on its wetted area, and the centerbody weight model depends on the maximum takeoff weight (MTOW); the areas of the pressurized cabin, flight deck, cargo holds, and unpressurized aft-centerbody; and the taper ratio of the area behind the cabin [35].

The airframe CG and inertias are estimated based on the shell centroid, assuming a homogeneous material distribution in the OML. All inertias are computed in the aircraft body frame at the end of each optimization iteration. The fuel weight is centered at the wing volume centroid, the payload weight acts at the volume centroid of the cabin,

Table 2 Comparison of OpenVSP and Jetstream planform parameters

Parameter	OpenVSP	Jetstream
Projected span [ft]	130.64	130.89
Projected area [ft ²]	2,654	2,667

**Fig. 2 Isometric view of a reconstructed BWB.**

and the fixed weights act through the shell centroid of the centerbody. As for flight mechanics, the static margin, given by $K_n = -C_{m_\alpha}/C_{L_\alpha}$, is calculated by approximating C_{m_α} and C_{L_α} through first-order forward finite differences with an angle-of-attack step size of $\Delta\alpha = 0.1^\circ$, using the CG as the moment summation point. Similarly, the static lateral-directional stability derivatives C_{n_β} and C_{l_β} are calculated by perturbing the sideslip angle β by 0.1° . The TOFL and other takeoff and initial-climb parameters are calculated by integrating the equations of motion developed based on FAR Part 25.

5. Gradient-Based Optimizer

The quasi-Newton optimizer SNOPT has been integrated with Jetstream [36]. The gradients of the objective function and flow-dependent constraints are evaluated using the discrete-adjoint method [37], with partial derivatives computed analytically or via the complex-step method [38]. The linear system of adjoint equations is solved using the iterative GCROT method to a tight relative tolerance of 10^{-8} to ensure accurate gradients. Optimization runs are deemed converged once the maximum nonlinear constraint violation is reduced to 10^{-6} , the first-order optimality is on the order of 10^{-4} , and the change in the merit function is on the order of 10^{-5} across five consecutive design iterations.

B. Prediction of Handling Qualities

After obtaining an optimized geometry and its static stability derivatives from Jetstream, VSPAero is used to calculate the dynamic stability derivatives required to predict handling qualities. VSPAero is a potential-flow solver packaged with the open-source conceptual aircraft design tool OpenVSP [39], with the Prandtl-Glauert or 2nd-order Kármán-Tsien rule applied for compressibility corrections. Following the workflow of Chang [14], the first step is to recreate the OML by modelling it as a wing with user-defined airfoil sections defined at discrete spanwise stations. To accurately approximate the Jetstream OML in a semi-automated manner, fifteen sections are extracted along the half-span. Next, the span, root chord, tip chord, and sweep of each segment between adjacent sections are adjusted to match the planform of the exact optimized geometry. The dihedral of each segment is then varied to match the front profile. Table 2 illustrates the similarity between the actual and approximate OMLs for an example geometry, and Figure 2 shows an isometric view of the reconstructed aircraft in OpenVSP.

VSPAero provides both panel and vortex-lattice method (VLM) solvers, but only the latter was used, as it supports simulations with control surface deflections. The VLM models the wing as a thin surface connecting the mean camber lines of each cross-section [40]. VSPAero also calculates stability derivatives using a finite-difference approximation, with a step size of 1 rad/s for rotation rates and 1 deg for angles. Despite the limitations of the VLM, it generates reasonably valid results for thin geometries under conditions where the flow is fully attached and the Mach number is low. While these assumptions are expected to hold at the low-speed operating point at which handling qualities are critical, the static directional stability derivative C_{n_β} computed by VSPAero agrees poorly with that computed by

Table 3 Requirements for the Dutch roll, spiral, and roll response at each level [16]

Level	Min ζ_{DR}	Min $\omega_{n,\text{DR}}$ [s ⁻¹]	Min $\zeta_{\text{DR}}\omega_{n,\text{DR}}$ [s ⁻¹]	$t_{\text{double, S}}$ (terminal flight) [s]	τ_{R} [s]
1	0.08	0.4	0.10	12	1.4
2	0.02	0.4	0.05	8	3.0
3	0	0.4	–	4	10

Jetstream. By neglecting cross-section thickness, the VLM underestimates the net destabilizing effect of the centerbody side area, which is biased ahead of the CG. Thus, only the dynamic stability derivatives from VSPAero are used in this work. Through a panel refinement study, the sensitivity of the Dutch roll eigenvalues to the panel density was determined to be low.

The lateral-directional equations of motion can be linearized about a trimmed equilibrium and formulated in the state-space form $\dot{\mathbf{x}} = \mathbf{A}\mathbf{x} + \mathbf{B}\mathbf{u}$, where \mathbf{x} is the state vector $[v, p, r, \phi]^T$, \mathbf{u} is the control input vector, the \mathbf{A} matrix represents the inherent dynamics of the aircraft and is a function of the dimensionalized stability derivatives, and the \mathbf{B} matrix represents how the control inputs influence the dynamics. The \mathbf{A} matrix is given by [41]:

$$\mathbf{A} = \begin{bmatrix} Y_v/m & Y_p/m & Y_r/m - V & g \cos \theta \\ L_v/I'_x + I'_{xz}N_v & L_p/I'_x + I'_{xz}N_p & L_r/I'_x + I'_{xz}N_r & 0 \\ N_v/I'_x + I'_{xz}L_v & N_p/I'_x + I'_{xz}L_p & N_r/I'_x + I'_{xz}L_r & 0 \\ 0 & 1 & \tan \theta & 0 \end{bmatrix} \quad (1)$$

where the pitch angle θ is assumed to be 0, and V is the speed at the equilibrium state. The primed inertia terms are:

$$I'_x = \frac{I_{xx}I_{zz} - I_{xz}^2}{I_{zz}} \quad I'_z = \frac{I_{xx}I_{zz} - I_{xz}^2}{I_{xx}} \quad I'_{xz} = \frac{I_{xz}}{I_{xx}I_{zz} - I_{xz}^2} \quad (2)$$

The inertia terms are computed in the body frame (b), which requires the following transformations to the stability frame (s) before assembling the \mathbf{A} matrix [41]:

$$\begin{aligned} I_{xx}^{(s)} &= I_{xx}^{(b)} \cos^2(-\alpha) + I_{zz}^{(b)} \sin^2(-\alpha) + I_{xz}^{(b)} \sin(-2\alpha) \\ I_{zz}^{(s)} &= I_{xx}^{(b)} \sin^2(-\alpha) + I_{zz}^{(b)} \cos^2(-\alpha) - I_{xz}^{(b)} \sin(-2\alpha) \\ -I_{xz}^{(s)} &= \frac{1}{2}(I_{xx}^{(b)} - I_{zz}^{(b)}) \sin(-2\alpha) + I_{xz}^{(b)}(\sin^2(-\alpha) - \cos^2(-\alpha)) \end{aligned} \quad (3)$$

where $-\alpha$ is the angle from the body x -axis to the stability x -axis, which aligns with the freestream. The moment derivatives are also computed in the body axes in Jetstream and VSPAero, and their transformations can be found in the Appendix.

The eigensystem of \mathbf{A} contains a complex-conjugate eigenvalue pair, which corresponds to the Dutch roll mode (DR), and two real eigenvalues corresponding to the spiral (S) and roll subsidence (R) modes, respectively. Key metrics can be derived from the eigenvalues:

- $\omega_{n,\text{DR}} = \sqrt{\Re(\lambda_{\text{DR}})^2 + \Im(\lambda_{\text{DR}})^2}$ is the Dutch roll natural frequency
- $\zeta_{\text{DR}} = -\Re(\lambda_{\text{DR}})/\omega_{n,\text{DR}}$ is the Dutch roll damping ratio
- the product $\zeta_{\text{DR}}\omega_{n,\text{DR}}$ represents the decay rate of the Dutch roll oscillations
- $t_{\text{double, S}} = \ln(2)/\lambda_{\text{S}}$ is the time to double for the spiral mode
- $\tau_{\text{R}} = 1/|\lambda_{\text{R}}|$ is the time constant for the roll subsidence mode

The military standard MIL-STD-1797A [16] classifies these metrics by levels, in which Level 1 denotes satisfactory handling qualities, Level 2, acceptable, and Level 3, controllable. The Dutch roll specifications applicable to medium-sized aircraft in low-speed, high-precision maneuvers are given in Table 3.

C. Motivation for Static Dutch Roll Proxies

Since Dutch roll involves coupled roll-yaw oscillations, this work investigates two lateral-directional static stability derivatives as proxies: the yaw stiffness C_{n_β} and dihedral effect C_{l_β} . An aircraft has static directional stability if it

produces a yaw moment that opposes the sideslip disturbance. Mathematically, this condition is given by $C_{n\beta} > 0$. The main contributor to $C_{n\beta}$ is the vertical stabilizer, since when $\beta \neq 0$, the component of V perpendicular to its chord line produces a side force that leads to a yaw moment about the CG. Improving directional stability through larger vertical stabilizers mitigates Dutch roll by minimizing sideslip excursions upon perturbation, thus limiting subsequent rolling due to the dihedral effect.

A positive roll angle ϕ about the x -axis is such that the new lift vector is rotated clockwise when viewed from behind. The aircraft must rotate counterclockwise about the x -axis to restore level flight, so $C_{l\phi} < 0$ is required for static roll stability. This is governed by $C_{l\beta}$ since a roll leads to a projection of the velocity vector in the spanwise direction, thereby inducing a sideslip angle β . The roll moment can be approximated by the truncated Taylor series $\Delta C_l \approx C_{l\beta}\beta$, where β is related to the angle of attack and roll angle. Applying the small-angle approximations for α and ϕ and differentiating with respect to ϕ yields $C_{l\phi} \approx C_{l\beta}\alpha$ [41]. It follows that a secondary condition for roll stability is $C_{l\beta} \leq 0$, since $\alpha > 0$ in most flight scenarios. Most transonic commercial aircraft satisfy this condition, as the wings are swept back, where the extent of sweep determines the difference in lift between each wing during a sideslip. Dihedral also enhances roll stability, since in a rolled orientation, the lower wing experiences a higher local angle of attack and produces more lift. A third factor is the wing root vertical position relative to the fuselage. On high-wing aircraft, the CG is below the wings and the fuselage functions as a pendulum, naturally maintaining level flight. Limiting the (negative) value of $C_{l\beta}$ will mitigate the sensitivity of the rolling moment to sideslip, thus inhibiting the onset of Dutch roll. What remains to be seen is how the individual and relative magnitudes of $C_{n\beta}$ and $C_{l\beta}$ translate into different levels of Dutch-roll handling qualities.

IV. Optimization Problem Formulation

This section highlights the salient features of the MDO problem formulation applied to the regional-class BWB aircraft. A more thorough description and justification of the design requirements can be found in Gray and Zingg [9].

A. Objective Function, Analysis Points, and Design Requirements

All optimization cases in this work seek to minimize block fuel burn, a system-level metric that aligns with the industry goal of simultaneously reducing greenhouse gas emissions and operating costs and does not rely on uncertain economic or climate-impact models. The design mission of the Embraer E190-E2, an equivalent best-in-class CTW, is used for sizing. Specifically, it consists of flying 3,100 nmi with 104 passengers at an initial cruise altitude of 36,000 ft and a Mach number of 0.78. At the start of cruise, the aircraft must be trimmed in lift and pitching moment.

In addition to the design point, two off-design analysis points are included in the problem formulation to impose critical design requirements stemming from the regulations. The first is on-ground OEI takeoff, which serves to size and position the vertical surfaces. The aircraft must achieve directional trim at the minimum control speed of 97 kt by deflecting the rudders to compensate for the asymmetric thrust. The second is low-speed approach outside of ground effect, at which static stability and lift generation are challenging. Trim and a minimum static margin of -4% MAC are enforced. To ensure a margin of safety, these constraints are imposed under the conservative and destabilizing conditions of aftmost CG, MTOW, takeoff safety speed, and zero thrust [9]. On variants of the baseline presented in Section V, static directional stability, namely a positive $C_{n\beta}$, and relaxed roll stability, namely a reduction in the magnitude of $C_{l\beta}$, are also enforced at the low-speed analysis point based on the findings from Ref. [14]. In all cases, pivot-piston landing gear is used to help satisfy the takeoff requirements; hence no rotation constraint is enforced.

B. Design Variables and Constraints

Table 4 provides an overview of the design variables and specifies some relevant bounds. To allow flexibility in adjusting the span, sweep, and dihedral, each of the four segments of the aircraft has a leading-edge axial curve, for a total of 10 axial control points, as depicted in Fig. 1. The requirement of fitting a 7.6-ft tall and 15.5-ft wide cabin is a primary driver of the centerbody span and sweep. The cargo holds are required to fit inside the centerbody or the blending segment. The wing dihedral must remain positive but less than 4° . The wing root has the freedom to translate vertically since its position relative to the centerbody influences roll stability. As structural proxies, the winglet aspect ratio must not exceed 4, while the root and tip chord must exceed 5 ft and 3 ft, respectively.

Eleven effective FFD stations independently control twist. The winglet twist is linearly interpolated between endpoints to improve grid-deformation robustness with negligible cost to performance. The chord length is free at the outer edges of the centerbody, blending segment, wing, and winglet, while the section chord perturbations within

Table 4 Design variables and bounds

Design variable	Quantity per analysis point	Analysis points	Select bounds
Angle of attack	1	cruise, low speed	(cruise) $[-3^\circ, 3^\circ]$
Centerbody elevator	1	low speed	$[-20^\circ, 20^\circ]$
Flap-elevon	3	low speed	$[-12.5^\circ, 12.5^\circ]$
Rudder	2	OEI	$[-30^\circ, 30^\circ]$
Twist angle	11		
Section shape	220		Wing, winglet: $(t/c) \geq 0.8(t/c)_0$
Chord length	5		Wing tip chord ≥ 5 ft Winglet tip chord ≥ 3 ft
Segment span	4		Centerbody: span \geq cabin span Winglet: such that $AR \leq 4$
Segment sweep	4		
Wing dihedral	1		$[0^\circ, 4^\circ]$
Wing root vertical position	1		
Cabin x -displacement	1		10 ft forward, 1 ft back
Cabin z -displacement	1		
Cabin floor angle	1		$[-3^\circ, 3^\circ]$
OEW CG perturbation	1		$\pm 5\%$ MAC
Takeoff field length model	6		1650 ft, climbout angle $\geq 1.37^\circ$
Engine scaling factor	1		
Thrust line angle	1		$\pm 2^\circ$
Total	266		

the centerbody are interpolated to preserve a rounded nose and avoid separation-prone wedge shapes under sideslip. The wing and winglet taper linearly for manufacturability and consistency with the wing-weight model; the winglet taper also improves grid robustness. As a structural surrogate, the minimum thickness-to-chord ratios for the wing and winglet are limited to 80% of their initial values. To prevent artificial twist, fore and aft top-bottom control-point pairs move equally and oppositely. The main landing gear is assumed to be long enough to prevent tip-strike at a pitch and roll attitude that simulates a destabilized final approach. Finally, 57.6% of wing volume (excluding a 5-ft tip margin) must exceed the fuel volume at maximum fuel weight.

The aircraft can trim by adjusting the angle of attack and deflecting the control surfaces. At cruise, the aircraft is trimmed with zero control surface deflections. At OEI on the ground, there is no need to enforce lift and pitch trim constraints. The rudders can deflect up to their full range of $\pm 30^\circ$ to achieve directional trim. At low-speed approach, the allowable deflection limits of the centerbody elevator and wing flap-elevons are conservatively set to 80% and 50% to safeguard against pitch saturation under more extreme flight conditions. Other constraints include cabin placement to maintain pilot visibility and limit the cruise deck angle, takeoff and initial climb performance, engine thrust-line angle and scaling factor, and OEW CG perturbations to account for future strategic systems layout decisions.

V. Results

This section presents the results of design sensitivity studies to individual and combined constraints on static lateral-directional stability derivatives. All performance, geometry, and stability-related characteristics are summarized in Table 5. Post-optimization dynamic stability analyses are performed at the trimmed low-speed angle of attack listed in Table 5 to assess the effectiveness of these constraints as proxy metrics for Dutch roll behaviour. Every optimized geometry has an active winglet aspect ratio constraint, is essentially shock-free at cruise, and exceeds the Level 1

MIL-STD-1797A specifications for the spiral and roll subsidence modes at low speed. As for the naming convention of the cases, the letters “NB” are used to denote a constraint on the yaw stiffness derivative $C_{n\beta}$, and “NLB” denotes constraints on both $C_{n\beta}$ and the dihedral effect derivative $C_{l\beta}$.

A. Baseline Characterization

To assess the dynamic lateral-directional stability in the absence of constraints on $C_{n\beta}$ and $C_{l\beta}$, a stability analysis at the trimmed low-speed angle of attack of 7.75 degrees, Mach 0.2, sea level, and MTOW is performed on the optimized baseline geometry B0. The stability derivatives (see Table 6) and mass properties are then compared to available data collected on the narrow-body jet airliner Convair 880 under similar operating conditions [42]. With a natural frequency $\omega_{nDR} = 0.969$ and damping ratio $\zeta_{DR} = 0.111$, the CV-880 exhibits Level 1 Dutch roll handling qualities. Thus, it serves as a suitable reference from which the drivers of adequate Dutch roll behaviour can be deduced.

From Table 5, B0 is unstable in Dutch roll, as evidenced by a negative damping ratio. Potential reasons can be inferred from Table 6, which shows that unlike the CV880, B0 exhibits an order of magnitude difference between $C_{n\beta}$ and $C_{l\beta}$, implying a strong imbalance between roll and yaw stability. The consequence for Dutch roll can be visualized when the aircraft is flying at a positive angle of attack and enters an uncoordinated roll to the right, inducing a sideslip angle to the right. Due to the swept-back wings, the lower right wing has a greater component of its span that is perpendicular to the relative wind, thereby generating more lift than the left wing and rolling the aircraft back to level flight. At the same time, the lower right wing also generates more lift-induced drag that causes it to yaw back, but the restoring yaw moment lags behind the roll, eventually leading to Dutch roll divergence.

The rate derivatives may also provide some insight into the Dutch roll response of B0. Assuming the oscillations are dominated by sideslip and yaw, the real part of the Dutch roll eigenvalue can be approximated to first-order using the following expression [41]:

$$\Re(\lambda_{DR}) = \frac{1}{2} \left[\frac{Y_v}{m} + I'_{xz} L_r + \frac{N_r}{I'_{zz}} + \frac{L_v/I'_{xx} + I'_{xz} N_v}{I'_{xz} L_v + N_v/I'_{zz}} \left(I'_{xz} L_p + \frac{N_p}{I'_{zz}} - \frac{g}{V} \right) \right] \quad (4)$$

Of the rate derivatives in (4), the greatest discrepancy between B0 and the CV-880 is in C_{n_r} , whose magnitude represents the resistance to a yawing motion and contributes to Dutch roll damping. Since C_{n_r} and its dimensional counterpart N_r are negative, increasing its magnitude shifts the Dutch roll eigenvalue to the left. Thus, the small magnitude of C_{n_r} on B0 could also be a source of poor Dutch roll damping. It should be noted that the rate derivatives are from the VLM solver, which does not account for the thickness of the centerbody. However, the main contributors to C_{n_r} are the wing aspect ratio, taper ratio, and sweep; and the moment arm and area of the vertical surfaces [41], which are independent of thickness.

Comparing the mass properties, I_{xz} is larger relative to I_{xx} and I_{zz} on B0 than the CV880, as for the latter, I_{xx} is 1.15×10^6 , I_{zz} is 4.07×10^6 , and I_{xz} is negligible. This indicates that relative to the CV880, B0 has greater mass asymmetry about the CG in the xz -plane and is expected to exhibit stronger roll-yaw coupling due to inertia. Consequently, an intended pure roll or yaw can initiate a Dutch roll.

The importance of static directional stability justifies the need to perform an optimization subject to an increased $C_{n\beta}$, both to quantify the cost to fuel burn and to determine whether it improves Dutch roll stability as a by-product. Subsequently, the dihedral effect requirement is relaxed by imposing a maximum $|C_{l\beta}|$ below the baseline value of -0.177. The individual and combined effect of this constraint with $C_{n\beta}$ on Dutch roll and its associated dynamic stability derivatives is studied. For now, since only the sensitivity of the Dutch roll handling qualities to these constraints is of interest, the constraints are imposed in the body axes and the bounds on these derivatives are arbitrary. Future work will seek to identify a range of values that enable adequate low-speed handling qualities with minimal fuel burn penalty.

Table 5 Performance and geometric characteristics of optimized variations

Parameter	B0	NB	NLB
BFB [lb]	20,246	20,490 (1.2%)	21,080 (4.1%)
MTOW [lb]	111,025	111,695 (0.6%)	112,165 (1.0%)
OEW [lb]	64,015	64,394 (0.6%)	64,168 (0.2%)
Centerbody	22,041	22,009 (-0.1%)	22,274 (1.1%)
Wings	9,358	9,600 (2.6%)	9,288 (-0.8%)
Winglets	551	674 (22.4%)	664 (20.55%)
Engines	8,066	8,111 (0.6%)	7,941 (-1.5%)
MZFW [lb]	86,895	87,274 (0.4%)	87,048 (0.2%)
MTOW I_{xx} [10^6 slug ft ²] ^a	1.087	1.129 (3.9%)	1.315 (21.0%)
MTOW I_{yy} [10^6 slug ft ²]	1.333	1.325 (-0.6%)	1.281 (-3.9%)
MTOW I_{zz} [10^6 slug ft ²]	2.343	2.384 (1.7%)	2.532 (8.1%)
MTOW I_{xz} [10^6 slug ft ²]	0.598	0.200 (-66.5%)	0.108 (-81.9%)
Span [ft]	126.42	128.04 (1.3%)	137.70 (8.9%)
Planform area [ft ²]	2,663	2,675 (0.4%)	2,802 (5.2%)
Wetted area [ft ²]	6,400	6,475 (1.2%)	6,683 (4.4%)
Wetted AR	2.50	2.53 (1.4%)	2.84 (13.6%)
Centerbody root chord [ft]	90.31	89.07 (-1.4%)	88.35 (-2.2%)
Wing leading-edge sweep [°]	35.27	35.69 (1.2%)	25.59 (-27.5%)
Wing dihedral [°]	4.00	0.00	0.00
Wing taper	0.312	0.300 (-4.0%)	0.300 (-3.9%)
Wing-only area	510.95	517.23 (1.2%)	565.87 (10.8%)
Wing-only AR	4.39	4.47 (1.8%)	4.89 (11.5%)
Winglet LE sweep [°]	37.30	38.18 (2.4%)	44.10 (18.2%)
Winglet height [ft]	18.12	19.99 (10.3%)	19.82 (9.4%)
Winglet taper	0.640	0.868 (35.6%)	0.85 (33.2%)
Cruise L/D	21.16	20.99 (-0.8%)	20.37 (-3.7%)
Cruise C_L	0.201	0.202 (0.2%)	0.193 (-4.0%)
Cruise C_D [cnts]	95.20	96.13 (1.0%)	95.0 (-0.3%)
Cruise angle of attack [°]	1.40	0.92	1.43
Cruise centerbody lift %	15.7	15.7 (0.1%)	18.8 (19.4%)
Low-speed C_L	0.706	0.707 (0.2%)	0.678 (-3.9%)
Low-speed angle of attack [°]	7.76	7.00	6.11
Low-speed centerbody lift %	20.1	19.9 (-0.7%)	20.7 (3.1%)
Low-speed elevator [°]	-20.00	-20.00	-20.00
Low-speed inboard elevon [°]	-12.50	-12.50	-12.50
Low-speed middle elevon [°]	0.43	-2.32	-12.50
Low-speed outboard elevon [°]	-2.20	0.65	12.00
Low-speed ω_{nDR} [rad/s]	0.768	0.731 (-4.7%)	0.631 (-17.9%)
Low-speed ζ_{DR}	-0.248	0.003	0.042
Low-speed $\zeta_{DR}\omega_{nDR}$ [rad/s]	-0.190	0.002	0.026
OEI rudder [°]	30.00	21.71	30.00

^a All inertias are calculated in the aircraft body frame with the CG as the reference point.

Table 6 Comparison of nondimensional sideslip and rate derivatives in the stability frame between the baseline BWB, its variants, and the Convair 880.

	$C_{y\beta}$	$C_{l\beta}$	C_{l_p}	C_{l_r}	$C_{n\beta}$	C_{n_p}	C_{n_r}
B0	-0.286	-0.177	-0.267	0.155	0.015	-0.049	-0.032
CV880	-1.015	-0.239	-0.395	0.309	0.145	-0.087	-0.218
NB	-0.311	-0.102	-0.268	0.158	0.026	-0.054	-0.042
NLB	-0.274	-0.078	-0.296	0.117	0.022	-0.039	-0.022

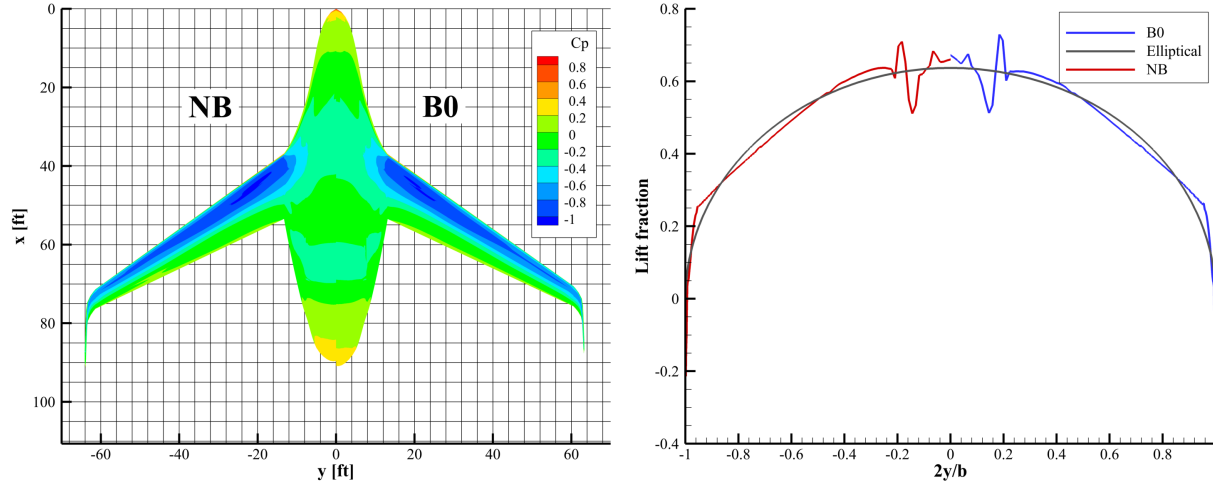


Fig. 3 Comparison of planforms and surface pressure coefficient distributions (left) and spanwise lift distributions (right) between cases B0 and NB at cruise.

B. Case NB: Sensitivity to a Yaw Stiffness Constraint

In the first variant of the baseline, the constraint $C_{n\beta} \geq 0.013^*$ was imposed at low speed. The effectiveness of this constraint as a static proxy for Dutch roll can be assessed by examining the damping ratio. Table 5 shows that it increases to a positive value corresponding to Level 3, indicating that constraining $C_{n\beta}$ could be a viable proxy to safeguard against Dutch roll instability. From Table 6, it induces design adaptations that reduce C_{n_r} and the magnitude of $C_{l\beta}$, both of which contribute to Dutch roll damping by pushing the real part of the eigenvalue to the left from (4). On the yaw control side, the rudder deflection at OEI is 8.3° less than that of the baseline, showing that the $C_{n\beta}$ constraint supersedes OEI directional trim as the driver of vertical surface sizing. Unlike on conventional aircraft, the engines on narrow-body BWBs are closer to the centerline due to being mounted at the rear of the centrebody, which mitigates the burden of OEI directional trim.

Despite the similarity of the B0 and NB planforms in Fig. 3, this constraint penalizes block fuel burn by 1.2%. The optimizer increases the winglet surface area by 21.3% through a 10.3% increase in its height and a 35.6% increase in its taper ratio, the latter as a result of the aspect ratio constraint. A 1.3% longer span and a 1.2% increase in wing sweep push the winglet centre of pressure back. Fig. 4 shows these design adaptations. While the wing centre of pressure would be shifted aft, the optimizer negates this effect by adjusting the section shapes and twist, which slightly front-loads the wing sections. Changes to the centerbody are inconsequential. The increase in the wing and winglet area drive up the overall wetted area, friction drag, and induced drag through the increase in airframe and fuel weight. Thus, the fuel burn penalty stems from a heavier aircraft and a lower L/D . Additionally, the dihedral decreases from the upper bound of 4° to the lower bound of 0° , contributing to a reduction in the magnitude of $C_{l\beta}$ by 43.5%, as seen in Table 6, and a 66.5% reduction in the product of inertia I_{xz} .

Since the $C_{n\beta} \geq 0.013$ constraint proved conducive to improving the Dutch roll damping at minimal cost to performance, the lower bound was tightened incrementally in an attempt to design a BWB that exhibits Level 1 Dutch

*Defined in the body frame

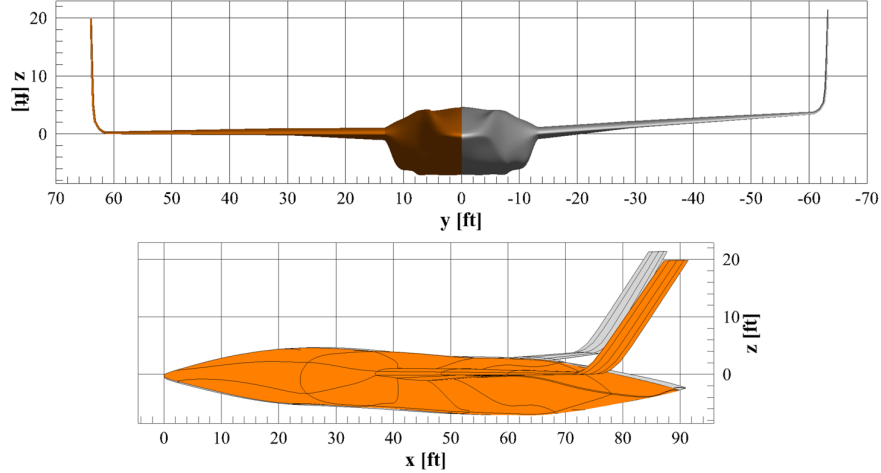


Fig. 4 Front and side views of B0 (gray) and case NB (orange).

roll handling qualities. In this problem formulation, where the aircraft is tailless and relies on winglets for directional stability, it was observed that the damping ratio only improves up to a certain point. First, the optimizer increases the winglet height and taper ratio and the wing tip chord while minimizing changes to other design variables. However, once the minimum $C_{n\beta}$ constraint exceeds a certain value, the winglet height and taper ratios reach their upper bounds, forcing the optimizer to sweep the wing further back to achieve a higher $C_{n\beta}$. This undermines the effectiveness of $C_{n\beta}$ as a proxy for Dutch roll, as $C_{l\beta}$ grows in magnitude with the increase in sweep, which is counterproductive to achieving well-damped oscillations. More broadly, it motivates the need to reconcile conflicting design adaptations on BWBs arising from the coupling of wing and winglet design and the tightly integrated airframe. One possible solution is to use centerbody-mounted fins for directional stability. Nonetheless, future studies should enforce a positive $C_{n\beta}$ at low speed within the baseline problem formulation since it is more critical for vertical surface sizing than OEI directional trim, but designers cannot rely solely on this constraint to ensure adequate Dutch roll handling qualities on the optimized geometry. Meanwhile, the performance penalty increases monotonically with a stricter $C_{n\beta}$ constraint, as the larger winglets and more highly-swept wings lead to a heavier airframe, consequently driving up induced drag, while the increase in wetted area drives up viscous drag.

C. Case NLB: Sensitivity to Combined $C_{n\beta}$ and $C_{l\beta}$ Constraints

In the second variant of the baseline, the constraint $C_{l\beta} \geq -0.08$ is imposed on top of the $C_{n\beta} \geq 0.013$ constraint to determine whether this combination of constraints is more effective than $C_{n\beta}$ alone at improving Dutch roll damping. The Dutch roll damping ratio of the optimized NLB aircraft is 0.042, indicating the effectiveness of this proxy. The natural frequency is reduced by 13.8% relative to NB, as the weakened dihedral effect results in a slower restoring roll response to a sideslip. The product of the damping ratio and natural frequency remain below the threshold for Level 2. The cost of fulfilling Level 2 damping criteria to block fuel burn is 2.9% relative to NB, reflecting the burden of the $C_{l\beta} \geq -0.08$ constraint. It is interesting to note that removing the $C_{n\beta}$ constraint does not appreciably change the optimal design, possibly because once the desired roll stability is achieved, the performance is less sensitive to a yaw stability requirement. In the future, a sweep of $C_{n\beta}$ and $C_{l\beta}$ can be performed to identify combinations of values that resolve the tradeoffs between adequate Dutch roll handling qualities and aerodynamic efficiency.

To reduce the dihedral effect[†], the wing sweep is reduced by 27.5%, as visualized in Fig. 5, and the wing root is shifted down relative to the centerbody, as visualized in Fig. 6. The lower sweep shortens the yaw moment arm, which makes the $C_{n\beta}$ constraint more challenging to satisfy. The optimizer compensates by pushing the wing root aft and elongating the span by 7.5%, driving an increase of 12.1% in the wetted aspect ratio. The winglets are swept back by an additional 15.5% while remaining the same size. Despite the higher wetted aspect ratio, the cruise L/D is reduced by 1.9% since the 4.8% increase in planform area reduces the cruise C_L . The downward twist of the inboard wing sections also reduces span efficiency and shifts the cruise spanwise lift distribution inboard, which is reflected in Fig. 5 and the 19.3% increase in the cruise centerbody lift fraction. The net effect of all design adaptations is a 46.1% reduction in I_{xz} ,

[†]All % changes in this paragraph are relative to NB unless otherwise stated.

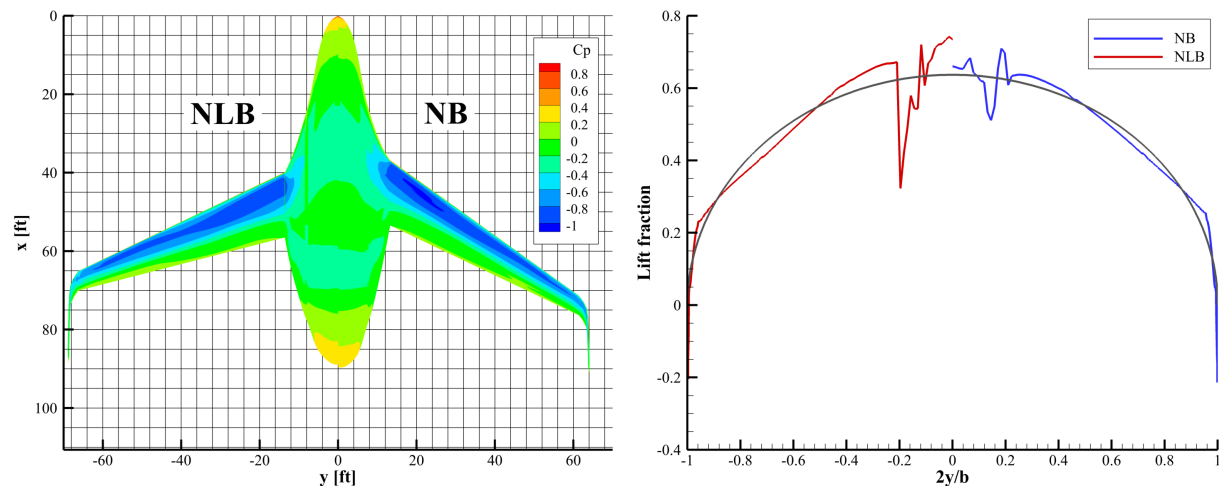


Fig. 5 Comparison of planform and surface pressure coefficient distribution (left) and front view and spanwise lift distribution (right) between cases NB and NLB.

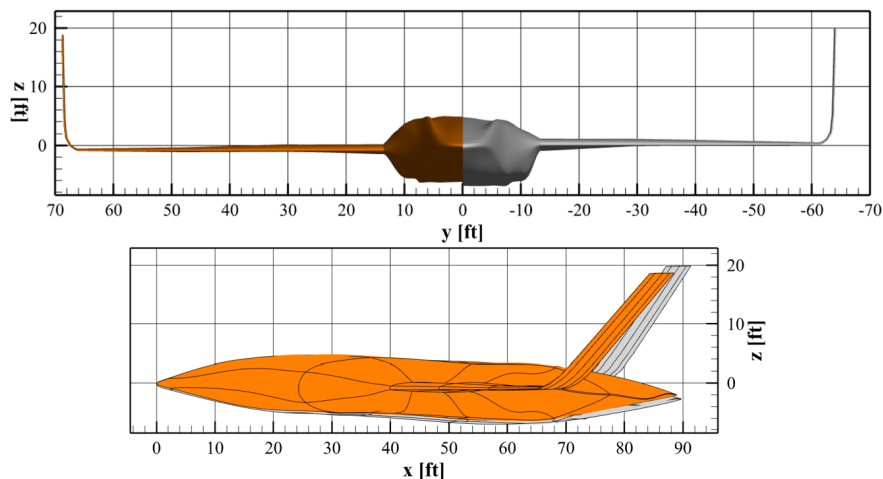


Fig. 6 Front and side views of cases NB (gray) and NLB (orange).

which further reduces the roll-yaw coupling due to inertia from B0. Table 5 shows that at low speed, the control surface deflections approach their operating limits. Fully deflecting the elevator and inboard and middle elevons down helps the optimizer minimize the area required to generate lift at low-speed, while deflecting the outboard elevon up creates washout, which helps with longitudinal trim in the presence of planform changes made to satisfy lateral-directional stability requirements. Unlike in case NB, the OEI rudder deflection is at its operational limit of 30° , as the lower sweep resulting from a weaker dihedral effect forces the rudder to be fully loaded.

VI. Conclusions

This paper introduces constraints on the yaw stiffness and dihedral effect derivatives to MDO problems on a narrow-body regional-class BWB aircraft. These derivatives are chosen based on the predicted Dutch roll response of the optimized baseline aircraft following a dynamic analysis, as well as knowledge of their effects on Dutch roll. Their impact on the optimal designs and their performance is studied, along with their applicability as proxies for Dutch-roll handling qualities. More broadly, this work seeks to determine whether it is possible to design an aircraft stable in Dutch roll when only static derivatives can be computed in the optimization loop.

Enforcing a weaker dihedral effect in addition to a minimum yaw stiffness improves the Dutch roll damping ratio

significantly, bringing it from an unstable baseline value to Level 2. However, these constraints drive an increase in wetted area and weight, resulting in a 4.1% block fuel burn penalty. Imposing the yaw stiffness constraint only brings the damping ratio to Level 3 while penalizing block fuel burn by 1.2%. While this lower penalty is desirable, the improvement in damping plateaus as the yaw stiffness constraint is tightened due to limits on the size of the winglets, the sole mechanism to achieve directional stability. Thus, the optimizer resorts to design adaptations that adversely affect other stability derivatives that influence Dutch roll. Future work could focus on reducing the dependence of the vertical surface design on the wing, possibly by using fins, as this is expected to help resolve conflicting design adaptations that negate Dutch roll stability. Furthermore, the $C_{n\beta}$ and $C_{l\beta}$ constraint values could be varied following a design-of-experiments approach to find a combination that improves Dutch roll damping at minimal cost to performance. Alternatively, data-driven methods could be investigated to enable the calculation of dynamic stability derivatives that influence Dutch roll within the optimization loop.

Acknowledgements

This work is funded by Bombardier, Transport Canada, the Natural Sciences and Engineering Research Council of Canada (NSERC), and the University of Toronto. All results in this paper were computed on the Niagara supercomputer at the SciNet HPC Consortium, a part of the Digital Research Alliance of Canada. The authors are also grateful to Dr. Peter Grant and Sacha Potvin at the University of Toronto Institute for Aerospace Studies for contributing their knowledge and guidance on aircraft handling qualities.

A. Lateral-Directional Stability Derivative Transformations

The lateral-directional stability derivatives are transformed from the body to the stability axes as follows [41]:

$$\begin{aligned}
L_v^{(s)} &= L_v^{(b)} \cos(-\alpha) - N_v^{(b)} \sin(-\alpha) \\
L_p^{(s)} &= L_p^{(b)} \cos^2(-\alpha) - (L_r^{(b)} + N_p^{(b)}) \sin(-\alpha) \cos(-\alpha) + N_r^{(b)} \sin^2(-\alpha) \\
L_r^{(s)} &= L_r^{(b)} \cos^2(-\alpha) - (N_r^{(b)} - L_p^{(b)}) \sin(-\alpha) \cos(-\alpha) - N_p^{(b)} \sin^2(-\alpha) \\
N_v^{(s)} &= N_v^{(b)} \cos(-\alpha) + L_v^{(b)} \sin(-\alpha) \\
N_p^{(s)} &= N_p^{(b)} \cos^2(-\alpha) - (N_r^{(b)} - L_p^{(b)}) \sin(-\alpha) \cos(-\alpha) - L_r^{(b)} \sin^2(-\alpha) \\
N_r^{(s)} &= N_r^{(b)} \cos^2(-\alpha) + (L_r^{(b)} + N_p^{(b)}) \sin(-\alpha) \cos(-\alpha) + L_p^{(b)} \sin^2(-\alpha) \\
Y_p^{(s)} &= Y_p^{(b)} \cos(-\alpha) - Y_r^{(b)} \sin(-\alpha) \\
Y_r^{(s)} &= Y_r^{(b)} \cos(-\alpha) + Y_p^{(b)} \sin(-\alpha)
\end{aligned} \tag{5}$$

where the nondimensional stability derivatives are dimensionalized via:

$$\begin{aligned}
L_v &= \frac{qSbC_{l\beta}}{V} & L_p &= \frac{qSb^2C_{lp}}{2V} & L_r &= \frac{qSb^2C_{lr}}{2V} \\
N_v &= \frac{qSbC_{n\beta}}{V} & N_p &= \frac{qSb^2C_{np}}{2V} & N_r &= \frac{qSb^2C_{nr}}{2V} \\
Y_v &= \frac{qSC_{Y\beta}}{V} & Y_p &= \frac{qSbC_{Yp}}{2V} & Y_r &= \frac{qSbC_{Yr}}{2V}
\end{aligned} \tag{6}$$

References

- [1] "Aircraft Technology Roadmap to 2050," Tech. rep., International Air Transport Association, 2019.
- [2] Liebeck, R. H., "Design of the Blended Wing Body Subsonic Transport," *Journal of Aircraft*, Vol. 41, No. 1, 2004, pp. 10–25.
- [3] Chen, Z., Zhang, M., Chen, Y., Sang, W., Tan, Z., Li, D., and Zhang, B., "Assessment on Critical Technologies for Conceptual Design of Blended-Wing-Body Civil Aircraft," *Chinese Journal of Aeronautics*, Vol. 32, No. 8, 2019, pp. 1797–1827.

- [4] “14 CFR § 25.672 - Stability augmentation and automatic and power-operated systems,” <https://www.ecfr.gov/current/title-14/chapter-I/subchapter-C/part-25/subpart-D/subject-group-ECFR3ac3aa184c8c5a/section-25.672>, April 1970. Accessed: 2024-08-28.
- [5] Larrimer, B. I., *Beyond Tube-and-Wing: The X-48 Blended Wing-Body and NASA’s Quest to Reshape Future Transport Aircraft*, NASA, Washington, DC, 2020.
- [6] Vicroy, D., “Blended-Wing-Body Low-Speed Flight Dynamics: Summary of Ground Tests and Sample Results (Invited),” *AIAA Aerospace Sciences Meeting*, Orlando, FL, 2009. AIAA-2009-0933.
- [7] Lyu, Z., and Martins, J. R. R. A., “Aerodynamic Design Optimization Studies of a Blended-Wing-Body Aircraft,” *Journal of Aircraft*, Vol. 51, No. 5, 2014, pp. 1604–1617.
- [8] Reist, T. A., Zingg, D. W., Rakowitz, M., Potter, G., and Banerjee, S., “Multi-Fidelity Optimization of Hybrid Wing-Body Aircraft with Stability and Control Requirements,” *Journal of Aircraft*, Vol. 56, No. 2, 2019, pp. 442–456.
- [9] Gray, A. L., and Zingg, D. W., “Blended-wing-body regional aircraft optimization with high-fidelity aerodynamics and critical design requirements,” *Journal of Aircraft*, Vol. 61, No. 6, 2024, pp. 1775–1792.
- [10] Yang, S. L., Page, M. A., and Smetak, E. J., “Achievement of NASA New Aviation Horizons N+2 Goals with a Blended-Wing-Body X-Plane Designed for the Regional Jet and Single-Aisle Jet Markets,” *AIAA SciTech Forum*, Kissimmee, FL, 2018. AIAA-2018-0521.
- [11] Crispo, J., “JetZero: Groundbreaking ‘blended-wing’ demonstrator plane cleared to fly,” <https://www.cnn.com/travel/jetzero-pathfinder-subscale-demonstrator/index.html>, 2024.
- [12] Gray, A. L., “Mixed-Fidelity Optimization of Blended-Wing-Body Regional Aircraft with High-Fidelity Aerodynamics and Critical Design Requirements,” PhD thesis, University of Toronto, Toronto, ON, June 2025.
- [13] Mader, C. A., and Martins, J. R. R. A., “Computing Stability Derivatives and Their Gradients for Aerodynamic Shape Optimization,” *AIAA Journal*, Vol. 52, No. 11, 2014, pp. 2533–2546.
- [14] Chang, C. T., “Handling Qualities of a Regional-Class Hybrid Wing Body Aircraft,” Master’s thesis, University of Toronto, Toronto, ON, 2023.
- [15] Gray, A. L., Reist, T. A., and Zingg, D. W., “Further Exploration of Regional-Class Hybrid Wing-Body Aircraft Through Multifidelity Optimization,” *AIAA SciTech Forum*, 2021. AIAA-2021-0014.
- [16] “Flying Qualities of Piloted Aircraft, MIL-STD-1797A,” Tech. rep., US Department of Defense, August 2004.
- [17] Gauvrit-Ledogar, J., Tremolet, A., Moens, F., Méheut, M., Defoort, S., Liaboeuf, R., Morel, F., and Paluch, B., “Multidisciplinary Design Analysis and Optimization Process Dedicated to Blended Wing Body Configurations,” *33rd Congress of the International Council of the Aeronautical Sciences*, Stockholm, Sweden, 2022.
- [18] Mader, C. A., and Martins, J. R. R. A., “Stability-Constrained Aerodynamic Shape Optimization of Flying Wings,” *Journal of Aircraft*, Vol. 50, No. 5, 2013, pp. 1431–1449.
- [19] Cosenza, D., and Vos, R., “Handling Qualities Optimization in Aircraft Conceptual Design,” *17th AIAA Aviation Technology, Integration, and Operations Conference*, Denver, CO, 2017. AIAA-2017-3763.
- [20] Joosten, S., Stroosma, O., Vos, R., and Mulder, M., “Simulator Assessment of the Lateral-Directional Handling Qualities of the Flying-V,” *AIAA SciTech Forum*, National Harbor, MD, 2023. AIAA-2023-0906.
- [21] “Certification Specification and Acceptable Means of Compliance for Large Aeroplanes, CS-25,” Tech. rep., European Aviation Safety Agency, July 2019.
- [22] Cai, Y., Xie, J., Harrison, E. D., and Mavris, D. N., “Assessment of Longitudinal Stability-and-Control Characteristics of Hybrid Wing Body Aircraft in Conceptual Design,” *AIAA Aviation Forum*, 2021. AIAA-2021-2448.
- [23] Garmendia, D. C., Chakraborty, I., and Mavris, D. N., “Multidisciplinary Approach to Assessing Actuation Poser of a Hybrid Wing-Body,” *Journal of Aircraft*, Vol. 53, No. 4, 2016, pp. 900–913.
- [24] Garmendia, D. C., Chakraborty, I., and Mavris, D. N., “Method for Evaluating Electrically Actuated Hybrid Wing-Body Control Surface Layouts,” *Journal of Aircraft*, Vol. 52, No. 6, 2015, pp. 1780–1790.

- [25] Denieul, Y., Bordeneuve, J., Alazard, D., Toussaint, C., and Taquin, G., “Multicontrol Surface Optimization for Blended Wing–Body Under Handling Quality Constraints,” *Journal of Aircraft*, Vol. 55, No. 2, 2018, pp. 638–651.
- [26] Reist, T. A., Koo, D., Zingg, D., Bochud, P., Castonguay, P., and Leblond, D., “Cross-Validation of High-Fidelity Aerodynamic Shape Optimization Methodologies for Aircraft Wing–Body Optimization,” *AIAA Journal*, Vol. 58, No. 6, 2020, pp. 2581–2595.
- [27] Gagnon, H., and Zingg, D. W., “Geometry Generation of Complex Unconventional Aircraft with Application to High-Fidelity Aerodynamic Shape Optimization,” *AIAA Aviation Forum*, San Diego, CA, 2013. AIAA-2013-2850.
- [28] Hicken, J. E., and Zingg, D. W., “Aerodynamic Optimization Algorithm with Integrated Geometry and Mesh Movement,” *AIAA Journal*, Vol. 48, No. 2, 2010, pp. 400–413.
- [29] Lahteenmaa-Swerdlyk, T., and Zingg, D. W., “Robust Mesh Deformation for Aerodynamic Shape Optimization with Large Geometric Changes,” *AIAA SciTech 2026 Forum*, Orlando, FL, 2026.
- [30] Gagnon, H., and Zingg, D. W., “Two-Level Free-Form and Axial Deformation for Exploratory Aerodynamic Shape Optimization,” *AIAA Journal*, Vol. 53, No. 7, 2015, pp. 2015–2026.
- [31] Abbot, I. H., von Doenhoff, A. E., and Stivers, L., “Summary of Airfoil Data,” Tech. rep., NACA Langley, 1945.
- [32] Osusky, M., and Zingg, D. W., “A Parallel Newton-Krylov-Schur Flow Solver for the Navier-Stokes Equations Discretized Using Summation-by-Parts Operators,” *AIAA Journal*, Vol. 51, No. 12, 2013, pp. 2833–2851.
- [33] Allmaras, S. R., Johnson, F. T., and Spalart, P. R., “Modifications and Clarifications for the Implementation of the Spalart-Allmaras Turbulence Model,” *7th International Conference on Computational Fluid Dynamics (ICCFD7)*, Big Island, HI, 2012.
- [34] Torenbeek, E., *Synthesis of Subsonic Airplane Design*, Delft University Press and Kluwer Academic Publishers, Dordrecht, 1982.
- [35] Bradley, K. R., “A Sizing Methodology for the Conceptual Design of Blended-Wing-Body Transports,” Tech. rep., NASA Langley Research Center, September 2019.
- [36] Gill, P., Murray, W., and Saunders, M., “SNOPT: An SQP Algorithm for Large-Scale Constrained Optimization,” *Society for Industrial Applied Mathematics Review*, Vol. 47, No. 1, 2005, pp. 99–131.
- [37] Jameson, A., “Aerodynamic Design via Control Theory,” *Journal of Scientific Computing*, Vol. 3, No. 3, 1988, pp. 233–260.
- [38] Osusky, L., Buckley, H., Reist, T., and Zingg, D., “Drag Minimization Based on the Navier-Stokes Equations Using a Newton-Krylov Approach,” *AIAA Journal*, Vol. 53, No. 6, 2015, pp. 1555–1577.
- [39] McDonald, R. A., and Gloudemans, J. R., “Open Vehicle Sketch Pad: An Open Source Parametric Geometry and Analysis Tool for Conceptual Aircraft Design,” *AIAA SciTech Forum*, San Diego, CA, 2022. AIAA-2022-0004.
- [40] Anderson, J. D., *Fundamentals of Aerodynamics*, 5th ed., McGraw-Hill, New York, NY, 2011.
- [41] Etkin, B., and Reid, L. D., *Dynamics of Flight: Stability and Control*, 3rd ed., John Wiley and Sons, Inc., Toronto, 1996.
- [42] Heffley, R. K., and Jewell, W. F., “Aircraft Handling Qualities Data,” Tech. rep., National Aeronautics and Space Administration, 1972.